



# Numerical Study on Laminar Drag Reduction for Superhydrophobic Surfaces with Continuous V-Shaped Microstructures

Y. Xu<sup>1</sup> and C. Ruan<sup>1,2†</sup>

<sup>1</sup> School of Mathematics and Statistics, Henan University of Science and Technology, Luoyang, 471023, China

<sup>2</sup> Longmen Laboratory, Luoyang, Henan, 471003, China

†Corresponding Author Email: [ruanchunlei@haust.edu.cn](mailto:ruanchunlei@haust.edu.cn)

(Received April 4, 2022; accepted July 29, 2022)

## Abstract

Superhydrophobic surfaces have attracted great attention owing to their capacity of reducing fluid resistance. Most of the previous numerical simulations on drag reduction of the superhydrophobic surfaces have concentrated on the rectangular microstructures, whereas few studies have focused on the continuous V-shaped microstructures. Based on the gas–liquid two-phase flow theory and volume-of-field model, combined with the semi-implicit method for pressure-linked equations algorithm, the effects of laminar drag reduction for superhydrophobic surfaces with continuous V-shaped microstructures were numerically studied. Three different sizes of superhydrophobic microchannels with continuous V-shapes were simulated according to the experimental data. Results showed that the drag reduction effects of continuous V-shaped microstructures were mainly determined by the width of adjacent microstructures, with the height of the microstructures only having minimal influence. At the same time, the effects of drag reduction for superhydrophobic surfaces with continuous V-shaped microstructures were compared with those with V-shaped and rectangular microstructures. The results indicated that the effects of drag reduction for superhydrophobic surfaces with continuous V-shaped microstructures were obviously better than for those with V-shaped microstructures, whereas the superhydrophobic surfaces with rectangular microstructures were more effective in reducing their drag than those with V-shaped microstructures under the condition of the same shear-free air–water ratios. Therefore, in the preparation of superhydrophobic materials, the continuous V-shaped microstructures are recommended; in addition, increasing the microstructure width should be emphasized in the preparation of superhydrophobic materials with continuous V-shaped microstructures.

**Keywords:** Superhydrophobic surface; Laminar flow; Drag reduction; V-shaped microstructure; Flow field.

## 1. INTRODUCTION

Superhydrophobic surfaces have attracted great attention owing to their capacity of reducing fluid resistance in microfluidic and nanofluidic applications. Superhydrophobic surfaces usually consist of micropatterns, such as pillars or ridges, on a smooth surface that displays superhydrophobicity so that the contact angle between the droplet and the micropattern is larger than 150°. A Cassie state (Cassie and Baxter 1944) is maintained and the water does not completely contact the solid surface over flow, but forms an air–water interface with the gas between adjacent micropatterns, causing a concomitant reduction in wall shear stress and flow resistance. So far, the drag reduction technology of superhydrophobic surfaces has shown promising potential in

applications such as underwater vehicles (Lee *et al.* 2016; Monfared *et al.* 2019), bionic sharkskin swimsuits (Monfared and Alidoostan 2020), water injection in oil reservoirs (Ijaola *et al.* 2020), etc. Therefore, it is of great significance to study the drag reduction of superhydrophobic surfaces with flow field.

At present, a substantial amount of experimental studies on drag reduction in microchannels employing superhydrophobic surfaces have been conducted. An experimental flow cell was designed to measure the pressure drop and slip length by Ou *et al.* (2004). They obtained a slip length of 20  $\mu\text{m}$  and 40% pressure drop when the shear-free ratio approached 1. A confocal surface metrology system was used to observe the formation of the air–water interface between microposts. The researchers claimed that this was the primary mechanism accounting for laminar drag reduction. In addition,

Ou and Rothstein (2005) further extended their research to examine the surface slip velocity with micron resolution particle image velocimetry (PIV). They found that the key to reducing drag on superhydrophobic surfaces lied in the shear-free air–water interface slip and a maximum slip velocity of up to 60% of the average velocity in the microchannel. Choi and Kim (2006) used a cone-and-plate rheometer to explore the superhydrophobic microchannels with nanoscale microposts. They reported that the slip length was about 20  $\mu\text{m}$ . Wang *et al.* (2014) used PIV to measure the velocity slip near a wall and found that this value exceed 15% when using superhydrophobic microchannels. They also observed that the reason for drag reduction was the air which was trapped in the cavity.

Apart from experimental studies, extensive numerical simulation investigations of the flow in channels containing superhydrophobic surfaces with various patterns and parameters have also been conducted. Sadaoui *et al.* (2021) used CFD method to simulate the two-dimensional (2D) steady flow on the surface with corrugated bottoms. The results showed that the flow in the channel was greatly affected by the geometric parameters of the bottom. Cheng *et al.* (2009) investigated the effective sliding performance of different microstructures, such as longitudinal grooves and transverse grooves as well as holes and columns. They found that different microstructures had different drag reduction effects. They also explored the effects of Reynolds number, microstructure height, and shear-free fraction on drag reduction. Teo and Khoo (2010) paid special attention to superhydrophobic surfaces with periodic longitudinal and transverse grooves. They concluded that the effective slip length was greatly affected by the groove width, and the longitudinal groove was more effective for reducing drag compared to the transverse groove. Kevin (2007) studied the microchannel with the cavity parallel to the flow direction. They found that the total friction resistance decreased as the width-to-height ratio of the microchannel decreased. Their work showed that drag reduction could reach up 90% in laminar flows. Zhao (2006) studied a 2D microchannel with rectangular cavity in a laminar flow. They found that the nondimensional pressure drop, slip velocity, and slip length increased with the increase in the shear-free fractions. They also proposed that there was a critical value of curvature of the air–water interface. If it was less than the critical value, the drag reduction indicators increased with the increase in the curvature of the air–water interface. Song *et al.* (2012) carried out numerical simulations on the flow field on superhydrophobic surfaces. They found that the drag reduction rate increased with the increase in the air–water interface area ratio, whereas the influence of the cavity depth was not obvious. They also found that the drag reduction effect of the rectangular groove in microstructure was better than those exhibited by the V-shaped and U-shaped grooves. Cheng *et al.* (2017) conducted a numerical simulation on the Poiseuille flow. They found that the friction resistance coefficient decreased with the

increase in slip length. Samaha *et al.* (2011) analyzed the superhydrophobic surface containing randomly distributed microstructures. Results revealed that the random distribution of microstructures had a positive influence on drag reduction. Li *et al.* (2016) examined the superhydrophobic microchannels based on the parabolic air–water interface. They concluded that the pressure drop and the normalized slip length decreased with the enlarged parabolic height of the air–water interface. They also explored the performance of dovetail, rectangular, trapezoidal, and triangular cavity microstructures. Their studies showed that the drag reduction effects sequentially worsened. Numerical experiments on the V-shaped microstructures were carried out by researchers. Liu *et al.* (2016) studied the drag reduction effects of three typical ribs: V-shaped ones, spaced triangular ones and blade-shaped ones. They compared their drag reduction effects where the height-to-spacing ( $h/s$ ) is 0.5 and 1. Xu *et al.* (2021) explored the air flow on the surface of the V-shaped groove. They found that when the flow velocity was 25m/s and the nondimensional depth parameter was about 14, the best drag reduction effect was achieved. Gu *et al.* (2017) simulated the flow field on the surface of V-shaped grooves. The influence of the flow direction and the inclination angles was investigated. It showed that the viscous resistance decreased significantly when the speed and inclination angle increased. Zhang *et al.* (2021) investigated the effect of the bionic microstructure parameters including the height and intersection angle of microstructure. The results showed that the V-shaped ones achieved the best drag reduction rate at  $h/s=1$ , while for the zigzag microstructures, the optimum drag reduction rate can be achieved at  $h/s=0.5$  and the apex angle was  $40^\circ$ .

With regards to the fabrication technologies of superhydrophobic surfaces, superhydrophobicity is often improved by reducing the contact area between the liquid and solid. This strategy often leads to rough surface fragile and highly susceptible to abrasion, such as the rough surfaces with dovetail and rectangular microstructures as mentioned in previous. Therefore, the abrasion of superhydrophobic materials is an aspect that needs to be considered during fabrication. Wang *et al.* (2020a) used photolithography to fabricate a microstructure framework composed of a microscale inverted pyramidal cavity on a silicon substrate, which could bear a high pressure. Wang *et al.* (2020b) fabricated three superhydrophobic surfaces with microstructures of different sizes on the surface of high-density polyethylene using the melt hot-pressing method, which corresponded to different hot pressures. The boat-sailing experiment showed that the superhydrophobic surfaces displayed obvious drag reduction compared to classical no-slip walls.

Previous investigations have shown that the structural parameters of superhydrophobic surfaces significantly affect the drag reduction properties. Therefore, it is necessary to further investigate how to increase the drag reduction effect by improving

the microstructural parameters. With the development of micromachining technology (Sajjad *et al.* 2021), the microstructures of hydrophobic materials with good drag reduction effects and good abrasion were fabricated. *e.g.*, (Wang *et al.* 2020a) and (Wang *et al.* 2020b). In their works, the microstructures were simplified as continuous V-shaped ones. Moreover, most of the previous numerical simulations have concentrated on the rectangular microstructures, whereas few systematic numerical studies on the drag reduction effect of continuous V-shaped microstructures on the basis of existing new materials. Although some achievements have been made in the numerical works of V-shaped microstructures, they have disadvantages: researchers only selected a single fixed parameter to explore its drag reduction effects, and did not quantitatively analyze the main drag reduction mechanism of the V-shaped microstructures from the actual material size, so as to provide the theoretical basis for the manufacturing engineering; besides, the wear-resistant properties of the microstructures have also received much attention currently, but few work systemically evaluated the drag reduction effects of the V-shaped microstructures in actual wear. Therefore, this study aimed to examine the drag reduction for superhydrophobic surfaces with continuous V-shaped microstructures in the laminar flow more comprehensively and systematically by combining actual fabrication engineering and applications. The overall organization of this study is as follows: at the beginning, the drag reduction effects of superhydrophobic surfaces with continuous V-shaped microstructures, with the sizes from experimental materials prepared by Wang *et al.* (2020b), are discussed by numerical simulation, the influence of the relative width and depth of the continuous V-shaped microstructure on the drag reduction effect are then qualitatively analyzed. Subsequently, the drag reduction effects of rectangular, V-shaped, and continuous V-shaped microstructures with different shear-free ratios are analyzed. In addition, we also consider the variation of drag reduction effect during wear in the practical application of continuous V-shaped microstructure. Ultimately, certain conclusions are drawn, which may hopefully be useful for designing superhydrophobic surfaces.

## 2. MODELS AND ALGORITHMS

### 2.1 Physical Models

As shown in Fig. 1, the micropatterns were fabricated at different hot-pressing temperatures with different heights by Wang *et al.* (2020b). In our simulation, three-dimensional (3D) micropatterns are simplified as 2D microstructures, as shown in Fig. 2. Therefore, the flow in 2D microchannel with continuous V-shaped microstructures is studied. The fluid flow in the channel is assumed to be laminar, steady, and incompressible, where the upper wall is a smooth surface and the lower wall is a superhydrophobic surface with regular microstructures. The air is

trapped in cavities between adjacent microstructures and the water enters from the inlet and exits from the outlet.

To explore the influence of structural parameters, the length, height, and width of the microchannel are denoted by  $L$ ,  $H$ , and  $h$ , respectively. The shear-free (air–water) fraction is defined as  $\beta = (S - a)/S$ , with  $S = a + b$  being the period,  $a$  being the width of the microstructure,  $b$  being the width of the cavity. In the case of continuous V-shaped microstructure,  $b = S$ , therefore, the shear-free ratio  $\beta = 1$ .

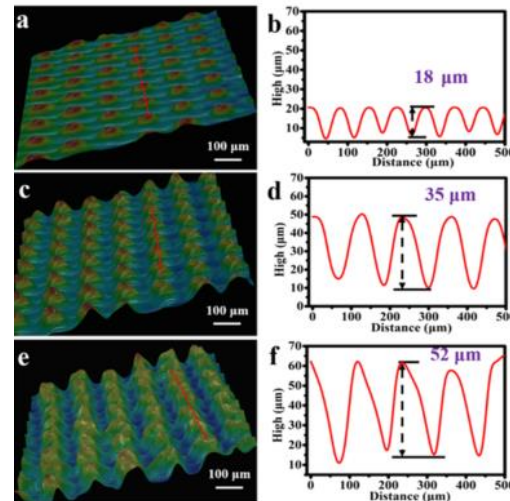


Fig. 1. 3D images of micropatterned surface and corresponding height of micropattern (Wang *et al.* 2020b).

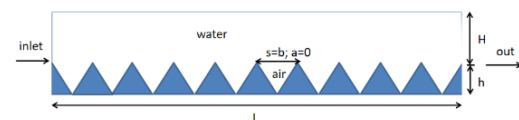


Fig. 2. Microchannel with continuous V-shaped microstructures

### 2.2 Mathematical Models

As shown in Fig. 2, water flows over rough surfaces and air is trapped in cavities and forms a typical gas–liquid two-phase flow. Therefore, we can obtain the volume fraction of the fluid and the gas–liquid interface by using the volume-of-fluid (VOF) model.

The flow in the channel is assumed to be a fully developed laminar flow. Therefore, the fluid satisfies three conservation equations. Here we assume the fluid to be isothermal, so the continuity equation and momentum equation are the governing equations.

The continuity equation is (Anderson 1995)

$$\frac{\partial u}{\partial x} + \frac{\partial v}{\partial y} = 0 \quad (1)$$

and the momentum equation is (Anderson 1995)

$$\begin{aligned} \rho u \frac{\partial u}{\partial x} + \rho v \frac{\partial u}{\partial y} &= -\frac{\partial p}{\partial x} + \mu \left( \frac{\partial^2 u}{\partial x^2} + \frac{\partial^2 u}{\partial y^2} \right), \\ \rho u \frac{\partial v}{\partial x} + \rho v \frac{\partial v}{\partial y} &= -\frac{\partial p}{\partial y} + \mu \left( \frac{\partial^2 v}{\partial x^2} + \frac{\partial^2 v}{\partial y^2} \right). \end{aligned} \quad (2)$$

where  $u$  and  $v$  are the velocity in the  $x$ - and  $y$ -directions, respectively.  $P$  is the pressure,  $\rho$  is the density, and  $\mu$  is the viscosity coefficient. The density and viscosity coefficients are derived from the following mixing theorem:

$$\begin{aligned} \rho &= \alpha_w \rho_w + (1 - \alpha_w) \rho_a \\ \mu &= \alpha_w \mu_w + (1 - \alpha_w) \mu_a \end{aligned} \quad (3)$$

where  $\rho_w$ ,  $\mu_w$  are the density and viscosity coefficients of water, respectively,  $\rho_a$  and  $\mu_a$  are the density and viscosity coefficients of air, respectively.  $\alpha_w$  is the volume fraction of water. The control volume is filled with water at  $\alpha_w = 1$ , the control volume is filled with air at  $\alpha_w = 0$ , while there is both water and air in the control volume when  $0 < \alpha_w < 1$ . The VOF equation that satisfies the volume fraction is (Anderson 1995)

$$\frac{\partial \alpha_w}{\partial t} + u \frac{\partial \alpha_w}{\partial x} + v \frac{\partial \alpha_w}{\partial y} = 0 \quad (4)$$

The computational domain is shown in Fig. 2. The boundary conditions are set as follows: the inlet velocity is  $u_{in} = 0.2 \text{ m/s}$ ; the outlet pressure is constant  $P = 1 \text{ KP}$ , other walls are set as the non-slip boundary conditions (Tariq et al. 2020). The initial states are set as follows: the cavities are full of air and the channel is full of water. From the observation results of Ou et al. (2004), it can be found that the curvature of the gas-liquid interface is very small on such a small scale. Therefore, the gas-liquid interface is assumed to be flat in this paper. The volume fraction diagram is shown in Fig. 3. The initial states are set as follows: the cavities are full of air and the channel is full of water.

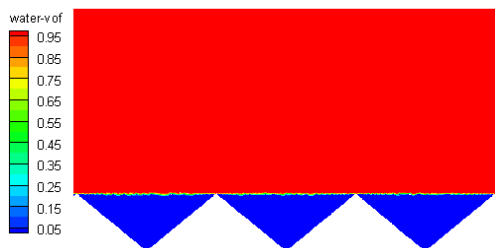


Fig. 3. Fraction contour with continuous V-shaped microstructures.

The semi-implicit method for pressure-linked equations algorithm (Tao 2001) is employed for coupling velocity and pressure, and the flow interface between air and water fluids are captured using the VOF model. The momentum equations are discretized using a second-order upwind scheme, the momentum residual is set as  $10^{-7}$ .

### 2.3 Nondimensional Pressure Drop Ratio and Normalized Effective Slip Length

To measure the drag reduction performance of superhydrophobic surfaces, it is essential to know the nondimensional pressure drop ratio and the normalized effective slip length.

The nondimensional pressure drop ratio is defined as follows (Ou et al. 2004)

$$\Pi = \frac{\Delta P_S - \Delta P}{\Delta P_S} \quad (5)$$

Where  $\Delta P_S$  and  $\Delta P$  are the average pressure drops of the stable section in the microchannels with smooth and superhydrophobic surfaces, respectively.

The normalized effective slip length is defined as follows (Cheng et al. 2009)

$$\frac{\lambda}{(H/2)} = \frac{32}{f \text{ Re}} - \frac{1}{3} \quad (6)$$

where  $f \text{ Re}$  is the Poiseuille number, which can be expressed as follows (Li et al. 2016)

$$f \text{ Re} = \frac{2 \Delta P D_h^2}{u_{in} \mu B} \quad (7)$$

where  $D_h = 2H$  is the channel hydraulic diameter and  $B$  is the microchannel length corresponding to the pressure drop. The Poiseuille number can also be employed for measuring the drag reduction effect.

## 3. RESULTS AND DISCUSSION

### 3.1 Validation

To investigate the validity of the numerical simulation in this work, preliminary computations were carried out. The numerical results of the flow in a smooth microchannel with the theoretical solution as well as the flow in a microchannel with a rectangular microstructure with the experimental solution were compared.

#### 3.1.1 Flow in smooth microchannel

The theoretical value of the Poiseuille number is constant between two infinite parallel plates, namely,  $f \text{ Re} = 96$ . A numerical simulation was carried out in a smooth microchannel with the length being  $L = 1800 \mu\text{m}$  and the height being  $H = 127 \mu\text{m}$ . The comparison between the simulated and the theoretical values is shown in Fig. 4. Here, the simulated value can be deduced from Eq. (7), where  $\Delta P$  is the pressure drop of the microchannel at the middle stable segments of  $500 \mu\text{m}$  and  $1500 \mu\text{m}$ . From Fig. 4, it can be observed that the simulated value agrees very well with the theoretical value, which indicates the reliability and accuracy of our simulations.

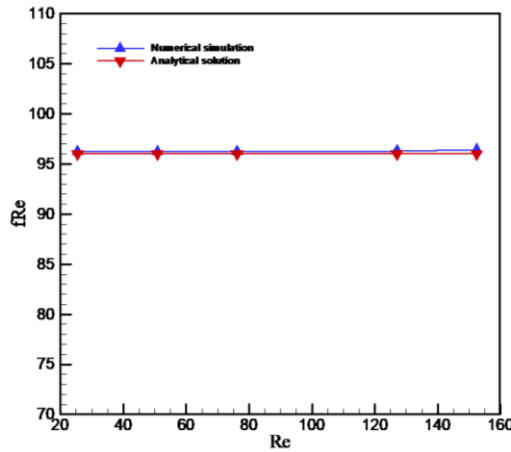


Fig. 4. Variation of the Poiseuille number  $f Re$  with the Reynolds number.

### 3.1.2 Flow in the rectangular microstructure channel

To further verify the validity of the model and algorithm, a numerical simulation was carried out in a microchannel with rectangular microstructure. *Ou et al. (2004)* performed the experiments in such a microchannel and obtained experimental data.

The physical model is shown in Fig. 5. The parameters we used in the simulation are as follows: length  $L = 1800\mu m$ , height  $H = 127\mu m$ , width of microstructures  $a = 30\mu m$ , and height of microstructures  $h = a$ . The cavity width  $b$  is taken as  $15\mu m, 30\mu m, 60\mu m, 150\mu m$ , respectively,  $\beta = (S - a)/S$ . As shown in Fig. 6, a structured grid is adopted and a local refinement is performed in the area where the flow field significantly changed. The grid numbers are  $4 \times 10^4 \sim 7 \times 10^4$  for four cases of cavity widths that we investigated.

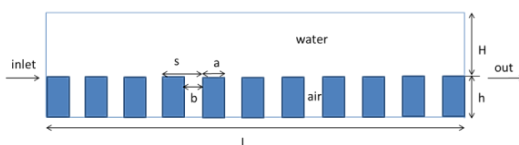


Fig. 5. Microchannel with rectangular microstructure model.

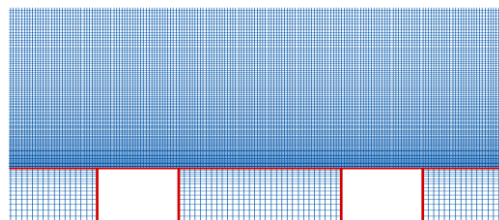
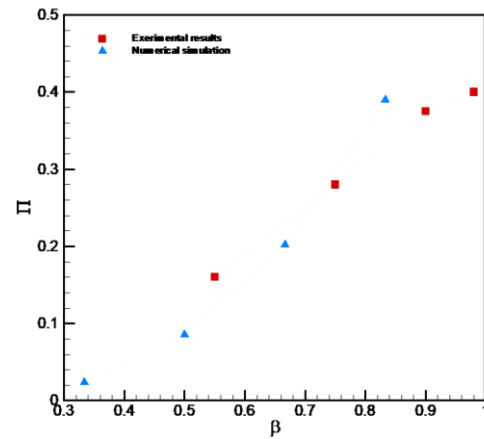


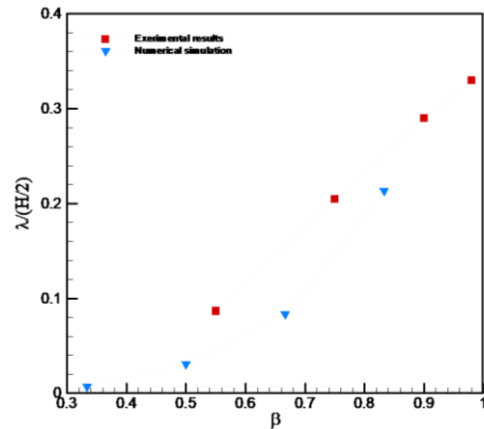
Fig. 6. Local grid diagram in the channel of rectangular microstructure.

Figure 7 presents the comparison between the simulated nondimensional pressure drop ratio and

the normalized effective slip length with the experimental results obtained by *Ou et al. (2004)*. The experimental and the simulation results show a good agreement. The average relative errors of the nondimensional pressure drop ratio and the normalized effective slip length are 4.49% and 7.69%, respectively. The deviation may be attributed to the fact that the experimental data is obtained in 3D microchannels, whereas the simulation in this study is carried out in 2D. Fig. 7 also reveals that the nondimensional pressure drop ratio and the normalized effective slip length increase with the increase in the shear-free fraction  $\beta$ .



(a) Nondimensional pressure drop ratio



(b) Normalized effective slip length

Fig. 7. Variation of the drag reduction parameters with the cavity fraction.

### 3.2 Analysis of the Surface Drag Reduction Effect of the Continuous V-Shaped Microstructure

The surface drag reduction of the continuous V-shaped microstructures with the same sizes reported by *Wang et al. (2020b)* is studied via numerical simulations. The physical model we considered is shown in Fig. 5. The microchannel width and height are taken as  $L = 1500\mu m$  and  $H = 300\mu m$ , respectively. Other parameters are

shown in Table 1. The average pressure at  $x = 500\mu\text{m}$  and  $x = 1200\mu\text{m}$  in the stable segments are taken to discuss, the streamline of this segment is shown in Fig. 9 which shows that the fully developed laminar flow is achieved. An unstructured grid is adopted, and local refinement is carried out in the area where the flow field significantly changes, as shown in Fig. 8. The grid numbers are  $1 \times 10^5 \sim 2.2 \times 10^5$  for the four cases that are listed in Table 1.

**Table 1. Microstructure parameters from Wang *et al.* (2020b)**

Microstructure size( $\mu\text{m}$ ) Name	width $s$	height $h$
Virgin film	0	0
H-65	75	18
H-95	130	35
H-125	127	52

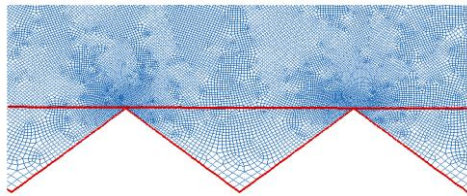


**Fig. 8. Local grid diagram in the channel with continuous V-shaped microstructures.**

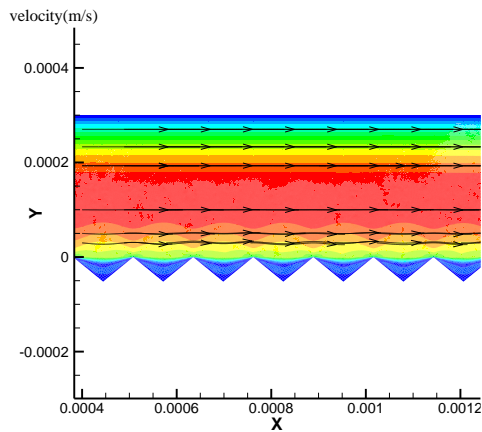


**Fig. 9. Local streamline plot.**

Figure 10 presents the velocity contour and velocity vector in the microchannel with a superhydrophobic surface of H-125 as listed in Table 1. Fig. 10(a) shows that the velocity field near the microstructure is very complicated, i.e., great velocity gradients are found in flow features from the solid-liquid to the air-water interface. The microstructure plays a very important role. Owing to the large viscous resistance near the solid-liquid interface, the velocity is very small and approaches zero near the wall. Meanwhile, the gas-liquid interface reduces the wall shear stress, which causes the slip velocity obviously, thereby leading to the reduction in resistance. Fig. 10(b) shows that the air is well

trapped in the cavity, and a low-speed whirl pool is produced inside. The flow direction of the vortex near the bottom of the cavity is opposite to the flow direction, while the flow direction of the vortex near the gas-liquid interface is consistent with the flow direction. Similar results are also reported by Song *et al.* (2012), who pointed out that the thrust effect and the vortex cushion effect were the main reasons accounting for the surface drag reduction.

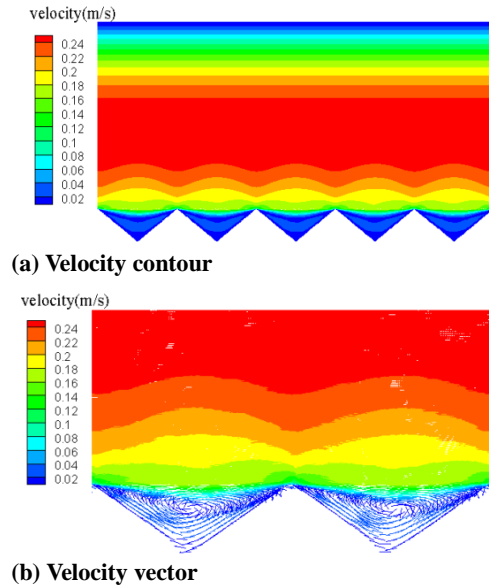


**Fig. 10. Velocity contour and velocity vector.**

In Table 2, the nondimensional pressure drop ratio, Poiseuille number, and normalized effective slip length are shown with the microstructure sizes listed in Table 1. The surface with continuous V-shaped microstructures can effectively reduce the drag, while the maximum nondimensional pressure drop and normalized effective slip length can reach more than 36% and 0.18, respectively. This is because the surface with a continuous V-shaped microstructure has a gas-liquid interface that has less viscous resistance compared with that of the original solid-liquid interface. Furthermore, Table 2 shows that the maximum nondimensional pressure drop and normalized effective slip length correspond to H-125. In other words, H-125 has the best drag reduction effect, which is consistent with the experimental results obtained by Wang *et al.* (2020b).

In Fig. 11, the slip velocities along the wall in a stable segment for three microstructure sizes and smooth microchannels are compared. As shown in Fig. 11, the slip velocity of the smooth microchannel is 0, while the slip velocity of H-125 is slightly higher than that of H-95. The slip velocity of H-125 and H-95 is larger than that of H-65, which agrees with the results in Table 2.

It can be known from the processing technology by Wang *et al.* (2020b) that the material was in a molten state at a high temperature, and the sample had completely reproduced the structure of the template. The height increased and the width

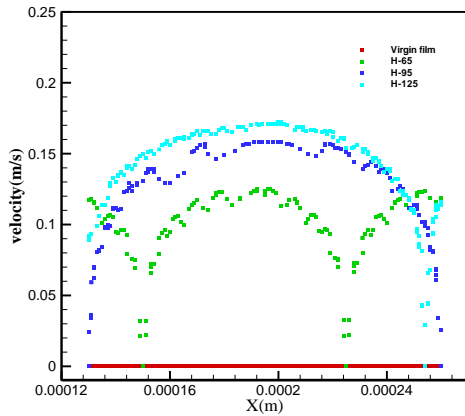


**Fig. 11. Comparison of slip velocity for three microstructures and smooth microchannel.**

**Table 2. Comparison of drag reduction with the parameters listed in Table 1**

Name	Non-Dimensional pressure drop ratio	Poiseuille number	Normalized effective slip length
Virgin film	0	97.1228	0
H-65	0.289	69.048	0.1301
H-95	0.3643	61.74	0.1849
H-125	0.3671	61.4684	0.1872

between adjacent microstructures slightly changed as pressure further increased. Therefore, here we assume that the microstructure width remains constant and the height continues to increase to investigate the influence on the effects of drag reduction. As shown in Fig. 12, the effect of microstructure height on nondimensional pressure drop ratio is not obvious. The nondimensional pressure drop ratio is stable around 36%. Thus, it can be concluded that the microstructure height has little influence on the drag reduction effect, which is consistent with the numerical results of Li *et al.* (2016).

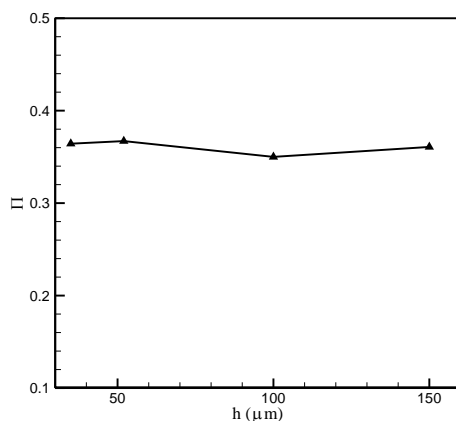


**Fig. 12. Variation in the nondimensional pressure drop ratio with the microstructure height.**

In general, via numerical analysis of the drag reduction effect of superhydrophobic surfaces with three microstructure sizes listed in Table 1 (Wang *et al.* 2020b), we obtained results consistent with the experimental data (Wang *et al.* 2020b), i.e.,  $H-65 < H-95 < H-125$ . In fact, the drag reduction effect of H-125 is only slightly better than that of H-95. As shown in Table 1, the three microstructures have different heights and widths. By comparing with the parameters of H-65 and H-95 in Table 1 and Table 2, it is obvious that the nondimensional pressure drop ratio and the normalized effective slip length increase with the increase in width and height. Both H-65 and H-95 positively affect the drag reduction effect, while H-95 has a larger influence. Table 2 shows that the nondimensional pressure drop ratio and the normalized effective slip length do not significantly change with H-95 and H-125. The parameters listed in Table 1 show that H-95 and H-125 have different heights but similar widths. Combining with the results in Fig. 12, we observe that the improvement of the drag reduction effect is mainly determined by the width of the adjacent microstructures, whereas the microstructure height only has a minimal influence.

Figure 13 shows the variation in the normalized effective slip length with the channel height. Here, we only increase the height  $H$  of the microchannel and retain other parameters, i.e., the microchannel length  $L=1500\mu m$ , cavity width  $s=127\mu m$ , and depth  $h=52\mu m$ . Fig. 12 shows that the normalized effective slip length decreases as the microchannel height  $H$  increases, the drag reduction effect is relatively weakened. The flow field features are plotted in Fig. 14. The superhydrophobic surface has a great influence on the whole flow field for the smaller height case. As the microchannel height increases, the influence of superhydrophobic surface on the flow field gradually decreases. When the microchannel height  $H$  reaches a certain value, the overall layered structure of the field is not affected, and the superhydrophobic surface only affects the flow field near the wall. This also indicates that the smaller the channel height, the more conducive it is for the drag reduction.

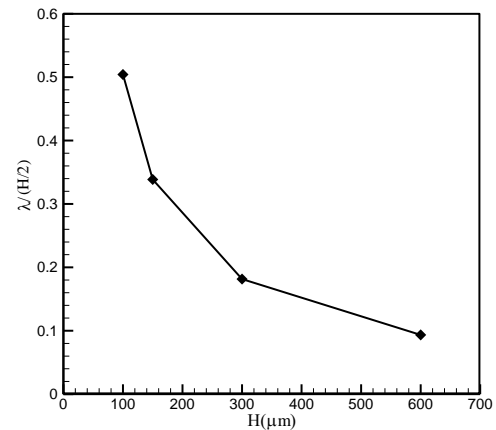


**Fig. 13. Variation in the normalized effective slip length with the channel height.**

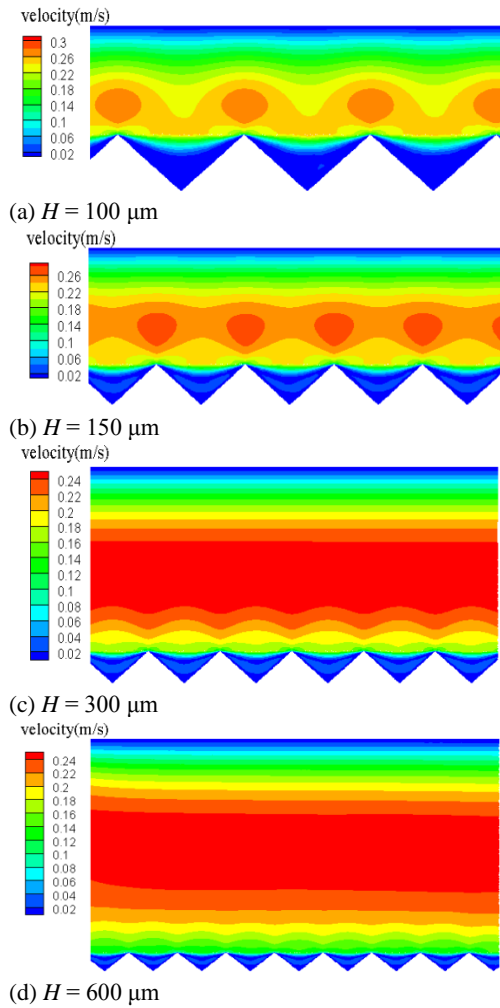


Fig. 14. Velocity contour at different microchannel heights.

### 3.3 Analysis of Surface Reduction Effect of Microstructure with Different Shapes

In this section, the surface drag reduction effects of microstructures with different shapes are analyzed. In fact, the continuous V-shaped microstructure is a special case of the V-shaped microstructure as shown in Fig. 15, i.e., a V-shaped microstructure with shear-free ratio  $\beta = 1$ . To further analyze the drag reduction effect of the continuous V-shaped microstructure, we compare the rectangular microstructure shown in Fig. 5 and the V-shaped microstructure shown in Fig. 15.

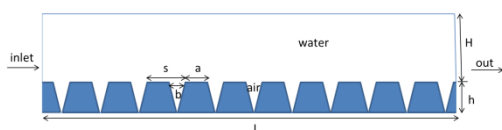


Fig. 15. Microchannel with V-shaped cavity model.

Numerical simulations were carried out in a

superhydrophobic microchannel with the parameters set as follows: length  $L = 1500 \mu m$ , height  $H = 300 \mu m$ , period  $s = 100 \mu m$ , and height of microstructure  $h = 50 \mu m$ . The average pressure at  $x = 500 \mu m$  and  $x = 1200 \mu m$  in the stable segments were taken to discuss.

The variations in the Poiseuille number and the normalized effective slip length with shear-free ratio in a microchannel containing V-shaped microstructures are shown in Fig. 16. It can be found that the Poiseuille number decreases with the increase in the shear-free area ratio, whereas the slip length increases with the increase in the shear-free area ratio. In addition, it is worth noting that when  $\beta < 0.9$ , the normalized slip length demonstrates a much milder increase when the shear-free ratio increases, whereas when  $\beta > 0.9$ , the effective slip length sharply increases as the shear-free ratio increases. The drag reduction effect is optimal at  $\beta = 1$ , while the slip length reaches 0.16. This indicates that the continuous V-shaped microstructures can demonstrate a better drag reduction effect.

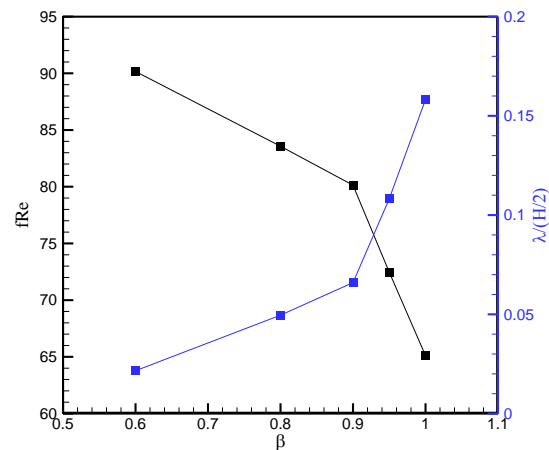


Fig. 16. Variation in the Poiseuille number and normalized effective slip length with shear-free ratio in V-shaped microstructure channels.

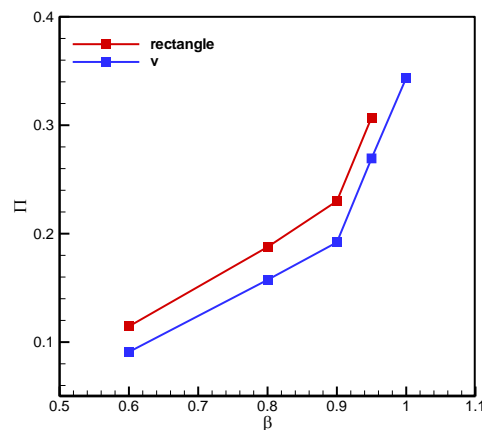


Fig. 17. Variation in the pressure drop with shear-free ratio for V-shaped and rectangular microstructures.

Figure 17 plots the nondimensional pressure drop ratio in the V-shaped microstructure and rectangular microstructure channel at different shear-free ratios. The results show that as the shear-free ratio increases, both the nondimensional pressure drop ratio and normalized slip length also increase. The nondimensional pressure drop ratio of the rectangular microstructure is larger than that of the V-shaped microstructure at the same shear-free ratio. This indicates that the drag reduction effect of the rectangular microstructure is better than that of the V-shaped one. This is consistent with the numerical results reported by Li *et al.* (2016) and Song *et al.* (2012). In addition, we also found that when the shear-free ratio  $\beta > 0.9$ , the nondimensional pressure drop ratio of the rectangular and the continuous V-shaped microstructures increased greatly with the increase of the no-shear ratio. In this case, increasing the width of adjacent microstructures has a more significant effect on the improvement of drag reduction. However, in engineering applications, the increased drag reduction by increasing the shear-free ratio also increases the wear resistance challenge for rough surfaces with microstructure, especially when the shear-free ratio is so high. As reported by Wang *et al.* (2020a), the continuous V-shaped microstructure demonstrated good wear resistance. Moreover, the nondimensional pressure drop ratio can reach 0.36 with the continuous V-shaped microstructure, which is beyond the reach of the rectangular microstructure that we simulated.

### 3.4 Analysis of the Change of Drag Reduction When the V-Shaped Microstructure is Worn

In practical applications, superhydrophobic surfaces are highly susceptible to mechanical wear, and abrasion may also alter the drag reduction effect of the surface (Tian *et al.* 2016). Therefore, in this section, the variation of drag reduction effect of V-shaped microstructures in actual wear are discussed.

Considering that in practical applications, at the initial stage of wear, the tip of the continuous V-shaped one will be smoothed, resulting in an “arc”, and the “arc” will gradually change as the degree of wear increases which are shown in Fig.18. Therefore, we perform smoothing at the tip to explore the drag reduction effect after wear.

Here, the quadratic Bezier curves with shape parameters are used to build the model in the early modeling. Let  $p_i (i=0,1,2)$  be the control point, then the quadratic Bezier curve with shape parameter is expressed as:

$$P(t) = \sum_{i=0}^2 p_i b_i(t)$$

where  $b_i(t)$  is the basis function:

$$\begin{cases} b_0(t) = 1 - \arcsin t + (arc - 1)\sin^2 t \\ b_1(t) = -arc + \arcsin t + \arccost \\ b_2(t) = arc - \arccost + (1 - arc)\sin^2 t \end{cases} \quad 0 \leq t \leq \frac{\pi}{2},$$

“arc” is a shape parameter that controls the shape of the curve, the control points of  $p_i (i=0,1,2)$  are shown in Fig. 18.

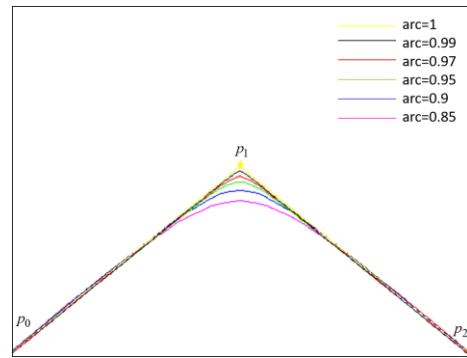


Fig. 18. Schematic diagram of parameter “arc”.

As shown in Fig. 18,  $arc=1$  is the initial continuous V-shaped one with cusps. The top radius of the microstructure changes gradually with the increase of wear degree while the parameter of arc gradually decreases. Fig. 19 plots the variation in the pressure drop with “arc” for continuous V-shaped microstructure. It can be seen from Fig.19 that the nondimensional pressure drop ratio gradually increases and then decreases with the decrease of the parameter of arc. When  $arc=0.99$ , the nondimensional pressure drop ratio reaches the maximum and exceeds 0.39. This may be due to the fact that the smooth top decreases the viscous resistance since it has no singularities in the calculation. However, as the parameter of arc decreases, the nondimensional pressure drop ratio gradually decreases, and the drag reduction effect gradually deteriorates. This may be because the reduction of air-water interface which increase the

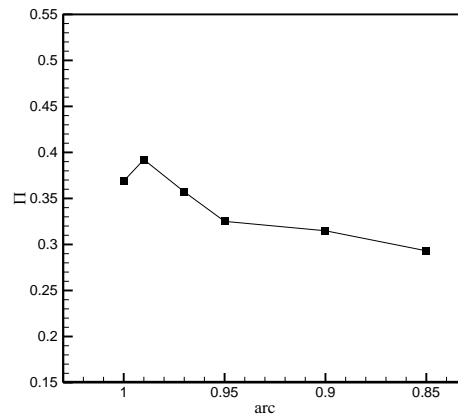
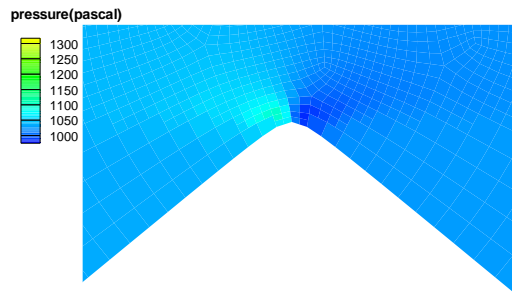


Fig. 19. Variation in the pressure drop with arc for continuous V-shaped microstructure.



**Fig. 20. Pressure contour at the tip of the continuous V-shaped microstructure.**

viscous resistance. The pressure contour at  $\text{arc}=0.99$  is shown in Fig. 20. As can be seen from Fig.20 that the pressure changes obviously near the top.

With increasing wear intensity or the effect of nanoparticles in water flow, the tip will be directly ground which means the height of the structure will decrease, but the bottom will remain unchanged until the surface loses its superhydrophobicity (Tian *et al.* 2016). In order to explore the influence of the microstructure on the drag reduction effect during the wear process, we take four different heights in the same microstructure to explore the variation of the drag reduction which are shown in Fig. 21.

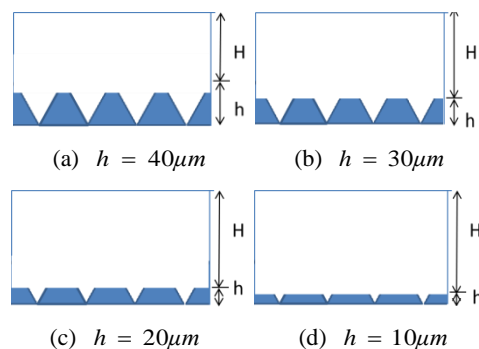


**Fig. 21. Microchannel with decreasing the microstructure height  $h$  during the wear.**

Figure 22 shows the variation of the nondimensional pressure drop ratio with decreasing the microstructure height. From the Fig. 22, it is clear that the nondimensional pressure drop ratio decreases with the decrease of the height of the microstructure; in addition, the superhydrophobic property is not so obvious in the case of  $h = 10\mu\text{m}$ . This may be caused by two reasons. One reason is that the height of the microstructure decreases during the wear, but the substrate remains unchanged which results in a proportional decrease in the gas-liquid contact surface and a proportional increase in the solid-liquid contact surface, thus the viscous resistance increases. Another reason may be that as the microstructure height  $h$  decreases, the relative height  $H$  of the microchannel increases, and the superhydrophobic surface has less influence on the microchannel.

To sum up, when the V-shaped microstructure is

slightly worn, that is, when the tip just begins to be rounded, it is beneficial to reduce the drag in the microchannel; however, with the continuous increase of the wear of the tip, the viscous resistance increases gradually which results in the worse drag reduction effect.

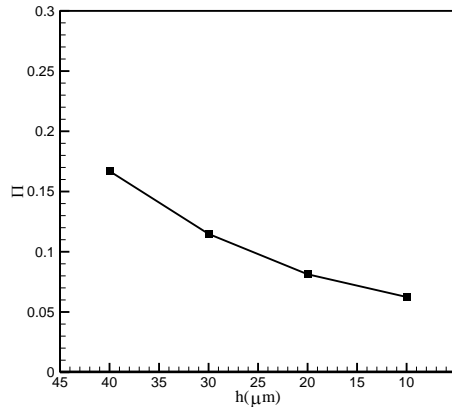


**Fig. 22. Variation of nondimensional pressure drop ratio with decreasing microstructure height  $h$ .**

#### 4. CONCLUSIONS

In this study, numerical simulations were performed to study the drag reduction effects of superhydrophobic surfaces with continuous V-shaped microstructures, using the parameters derived from the experiments (Wang *et al.* 2020b). Meanwhile, the drag reduction effects of the patterned superhydrophobic surfaces containing rectangular, V-shaped, and continuous V-shaped microstructures were analyzed. Finally, the drag reduction effect of the continuous V-shaped microstructure after wear is briefly analyzed. The main conclusions are summarized as follows.

(1) The simulation results in this study are consistent with the experimental results (Wang *et al.* 2020b), i.e.,  $H-65 < H-95 < H-125$ . The drag reduction effect of H-125 is only slightly better than that of H-95. The adjacent pattern width greatly affects the drag reduction effect, whereas the microstructure height has little influence on it. In the superhydrophobic surface with continuous V-shaped microstructures, the microstructure width corresponds to the cavity width. When the width increases, the relative area of the air-water interface increases correspondingly, causing the reduction in viscous resistance. Thus, the drag reduction effect is improved. Therefore, in the preparation of superhydrophobic materials with continuous V-shaped microstructures, the focus should be on increasing the microstructure width.

(2) The effects of drag reduction in superhydrophobic surfaces with continuous V-shaped microstructures are obviously better than those with V-shaped microstructures. The superhydrophobic surfaces with rectangular microstructures can more effectively reduce their

drag than those with V-shaped microstructures, given the shear-free air–water ratios remain the same. When the shear-free ratio  $\beta > 0.9$ , the nondimensional pressure drop ratio changes more significantly with the increase of the shear-free ratio.

The superhydrophobic surfaces with continuous V-shaped microstructures with the shear-free ratio  $\beta = 1$  have a better drag reduction effect than those with rectangular microstructures that we simulated. And the worn continuous V-shaped microstructure with a slightly rounded tip has a better drag reduction effect, and its nondimensional pressure drop ratio exceeds 0.39. Therefore, in view of the wear resistance and drag reduction effects, the superhydrophobic surfaces with continuous V-shaped microstructures are suggested for drag reduction.

### ACKNOWLEDGMENT

The authors acknowledge the School of Mathematics and Statistics, Henan University of Science and Technology, for allowing the use of their high-performance computing resources.

### REFERENCES

- Anderson, J. D. (1995). *Computational fluid dynamics: the basics with applications* Tsinghua University Press, Beijing, China.
- Cassie, A. B. D. and S. Baxter (1944). Wettability of porous surfaces, *Transactions of the Faraday Society* 40(1), 546-551.
- Cheng, Y. L., Y. Jiang and Z. P. Xue (2017). Effects of slip length on the characteristics of Poiseuille microflow of liquid, *Journal of Engineering Thermophysics* 38(12), 7.
- Cheng, Y. P., C. J. Teo and B. C. Khoo (2009). Microchannel flows with superhydrophobic surfaces: Effects of Reynolds number and pattern width to channel height ratio, *Physics of Fluids* 21(12), 011701.
- Choi, C. H. and C. J. Kim (2006). Large Slip of Aqueous Liquid Flow over a Nanoengineered Superhydrophobic Surface, *Physical Review Letters* 96(6), 066001.
- Gu, Y. Q., T. X. Fan, J. G. Mou, D. H. Wu, S. H. Zheng and E. Wang (2017). Characteristics and Mechanism Investigation on Drag Reduction of Oblique Riblets, *Journal-Central South University* 24(6), 1379-86.
- Ijaola, A., P. K. Farayibi and E. Asmatulu (2020). Superhydrophobic Coatings for Steel Pipeline Protection in Oil and Gas Industries: A Comprehensive Review, *Journal of Natural Gas Science and Engineering* 83(8), 103544.
- Kevin, B. J. (2007). *Numerical Study of Fully Developed Laminar and Turbulent Flow Through Microchannels with Longitudinal Microstructures*, MA., Brigham Young University.
- Lee, C., C. H. Choi and C. J. Kim (2016). Superhydrophobic drag reduction in laminar flows: a critical review, *Experiments in Fluids* 57(12), 1-20.
- Li, C., S. Zhang, Q. Xue and X. Ye (2016). Simulation of drag reduction in superhydrophobic microchannels based on parabolic gas-liquid interfaces, *Physics of Fluids* 28(10), 102004.
- Liu, D. J., Y. Yu, G. F. Wang, M. M. Zhang and X. S. Li (2016). The Characteristic and Mechanism of Three Different Shapes of Riblets on Drag Reduction, *Journal Of Engineering Thermophysics* 37(7), 1411-15.
- Monfared, M. and M. A. Alidoostan (2020). Optimization of Drag Reducing Shark Inspired Blade-Shape Riblet Surfaces in External Flow, *Journal of Applied Fluid Mechanics* 13(1), 55-65.
- Monfared, M., M. A. Alidoostan and B. Saranjam (2019). Experimental Study on the Friction Drag Reduction of Superhydrophobic Surfaces in Closed Channel Flow, *Journal of Applied Fluid Mechanics* 12(1), 69-76.
- Ou, J., B. Perot and J. P. Rothstein (2004). Laminar drag reduction in microchannels using ultrahydrophobic surfaces, *Physics of Fluids* 16(12), 4635-4643.
- Ou, J. and J. P. Rothstein (2005). Direct velocity measurements of the flow past drag-reducing ultrahydrophobic surfaces, *Physics of Fluids* 17(10), 3606.
- Sadaoui, D., M. Bachir and K. J. C. E. C. Aimad (2021). Cfd Analysis of Natural Convection between Two Superposed Fluids: Role of Corrugated Bottoms, *Chemical Engineering Communications* 208(6), 1976162.
- Sajjad, U., A. Sadeghianjahromi, H. M. Ali and C. C. Wang (2021). Enhanced Pool Boiling of Dielectric and Highly Wetting Liquids – a Review on Surface Engineering, *Applied Thermal Engineering* 195, 117074.
- Samaha, M. A., H. Vahedi Tafreshi and M. Gad-El-Hak (2011). Modeling drag reduction and meniscus stability of superhydrophobic surfaces comprised of random roughness, *Physics of Fluids* 23(1), 012001.
- Song, B., X. Yuan and H. Hu (2012). Simulating flow field of superhydrophobic Surface in laminar flow to reduce its drag, *Journal of Northwestern Polytechnical University* 30(5), 712-717.
- Tao, W. (2001). *Numerical heat transfer (second edition)* Xi'an Jiaotong University Press, Xi'an, China.
- Tariq, H. A., M. Anwar, A. Malik and H. M. Ali (2020). Hydro-Thermal Performance of

- Normal-Channel Facile Heat Sink Using TiO<sub>2</sub>-H<sub>2</sub>O Mixture (Rutile-Anatase) Nanofluids for Microprocessor Cooling, *Journal of Thermal Analysis and Calorimetry* 145(2), 2487-502.
- Teo, C. J. and B. C. Khoo (2010). Flow past superhydrophobic surfaces containing longitudinal grooves: effects of interface curvature, *Microfluidics & Nanofluidics* 9(2-3), 499-511.
- Tian, X., T. Verho and R. Ras (2016). Moving Superhydrophobic Surfaces toward Real-World Applications, *Science* 352(6282), 142-43.
- Wang, B., J. Wang and D. Chen (2014). Drag reduction on hydrophobic transverse grooved surface by underwater gas formed naturally, *Acta Physica Sinica* 63(07), 214-220.
- Wang, D., Q. Sun, F.-Y. Lin, M. J. H. C. Zhang, Q. Liu, h.-P. Zhu, T. Zhou, Q. Chang, B. He, Q. Zhou, L. Chen, Z. Wang, R. H. A. Ras and X. Deng (2020a). Design of robust superhydrophobic surfaces, *Nature* 582(4), 55-59.
- Wang, Y., C. Gao, W. Zhao, G. Zheng and C. Shen (2020b). Large-area Fabrication and Applications of Patterned Surface with Anisotropic Superhydrophobicity, *Applied Surface Science* 529(6), 147027.
- Xu, Y., C. Zhang and Z. X. Wang (2021). Simulation Analysis on Drag Reduction Performance of Characteristic Parameters of V-Groove on Local Approximate Plane, *Aeronautical Manufacturing Technology* 64(15), 86-99.
- Zhao, J. J. (2006). 'Slip flow research in microchannels with superhydrophobic surface by experimental and numerical simulation methods', MA., Dalian University of Technology.
- Zhang, M. H., D. B. Zhang and W. W. Zhuo (2021). Research on Composite Drag Reduction Characteristics of Biomimetic Microstructural ,Surface *Journal of Applied Fluid Mechanics* 14(5), 1337-50.